Sea Level Pressure Anomalies in the Western Pacific during El Niño: Why are they there?

XUAN JI, J. DAVID NEELIN and C. ROBERTO MECHOSO

Department of Atmospheric and Oceanic Sciences, University of California, Los Angeles, Los Angeles, California

ABSTRACT

Although sea level pressure (SLP) anomalies in the Western Pacific have long been recognized as an integral part of the classic Southern Oscillation pattern associated with ENSO, there is an unresolved question regarding the dynamics that maintain these. Traditional studies of the ENSO response in the tropics assume a single deep baroclinic mode associated with the tropospheric temperature anomalies. However, the SLP anomalies in the western Pacific are spatially well separated from the baroclinic signal in the NCEP-NCAR reanalysis, CMIP5 models, and an intermediate complexity model [a quasi-equilibrium tropical circulation model (QTCM)]. Separation of the SLP anomalies into their baroclinic and barotropic components indicates that while the baroclinic components are fundamental contributors to ENSO anomalies in the central and eastern Pacific (coincident with the temperature anomalies), the barotropic components provide the primary contributions in the western Pacific.

To demonstrate the roles of baroclinic and barotropic modes in ENSO teleconnections within the tropics, a series of QTCM experiments is performed, where anomalies in the interactions between baroclinic and barotropic modes are suppressed over increasingly wider latitudinal bands in the tropical Pacific. If this suppression is done in the 15°N-15°S band, the pressure signals in the western Pacific are only partly removed, whereas if it is done in the 30°N-30°S band, the anomalies in the western Pacific are almost entirely removed. This suggests the following pathway: interactions with SST anomalies create the baroclinic response in the central and Eastern Pacific, but baroclinic-barotropic interactions, arising substantially in the subtropical Pacific, generate a barotropic response that yields the SLP anomalies in the western Pacific.

1. Introduction

El Niño/Southern Oscillation (ENSO) is associated with sea level pressure (SLP) anomalies that have long been recognized to form an oscillation pattern with poles in the western equatorial and southeastern Pacific (e.g., Walker 1923; Berlage 1957; Wallace et al. 1998). ENSO is also associated with tropospheric temperature anomalies that spread from the central and eastern Pacific in many ways that resemble basic equatorial wave dynamics (Kiladis and Diaz 1989; Wallace et al. 1998; Chiang and Sobel 2002; Su and Neelin 2002; Kumar and Hoerling 2003). Some major aspects of ENSO dynamics can be understood through conceptual models based on a single deep baroclinic mode that is separable from the barotropic mode in the absence of baroclinic advection and vertical turbulent momentum transport (Matsuno 1966; Webster 1972; Gill 1980). Therefore, highly damped shallow water models often give a plausible first approximation to the low level wind response in the immediate vicinity of ENSO convective heating anomalies. The SLP anomalies in the western tropical Pacific, however, are spatially well separated from the baroclinic signal associated with the tropospheric temperature anomalies over the central and eastern Pacific. The lack of associated temperature anomalies in the western Pacific suggests that baroclinic wave propagation is not the main driver of the SLP anomalies in the region. Therefore, the SLP response in this region must stem from the excitation of a barotropic mode.

The barotropic teleconnections from the ENSO heating region into mid-latitudes are well known (Horel and Wallace 1981; Hoskins and Karoly 1981; Simmons 1982; Branstator 1983; Simmons et al. 1983; Held and Kang 1987). Lee et al. (2009) have analyzed the baroclinic and barotropic responses to ENSO-like heating, as well as the importance of vertical background wind shear in exciting the barotropic response in mid-latitudes. In the present study we show that within the tropics, barotropic teleconnections excited by the baroclinic-barotropic interactions are responsible for the ENSO atmospheric response in SLP over the tropical western Pacific. Our hypothesis is the following: as baroclinic Rossby waves propagate west from the central and eastern equatorial Pacific, they excite barotropic wave trains through barotropic-baroclinic interactions. These wave trains can then propagate west to generate the SLP anomalies in the western Pacific, albeit the baroclinic mode propagation does not reach that region. The barotropic mode can be forced by three barotropic-baroclinic interaction terms: 1) shear advection (Wang and Xie 1996; Majda and Biello 2003; Biello and Majda 2004b), 2) surface drag (Neelin and Zeng 2000; Biello and Majda 2004a), and 3) vertical advection (Bacmeister and Suarez 2002). Recently, Ji et al. (2014) provided a detailed analysis of the effects these three terms have in interhemispheric teleconnections from tropical heat sources.

To demonstrate the respective roles of baroclinic and barotropic modes in ENSO teleconnections within the tropics, we first analyze the teleconnection patterns in the NCEP reanalysis and in several simulations done with general circulation models (GCMs) participating in phase 5 of the Coupled Model Intercomparison Project (CMIP5). Then to analyze the dynamics that maintain the SLP anomalies in western Pacific associated with ENSO, we perform a set of diagnostic experiments using a quasi-equilibrium tropical circulation model (QTCM), where the impact of the baroclinic-barotropic interaction terms on the SLP anomalies in the western Pacific can be artificially suppressed.

The remainder of the text is organized as follows. Section 2 gives a brief introduction of the datasets, model and methodology used in this study. Section 3 presents the analysis of ENSO tropical teleconnections in NCEP reanalysis and CMIP5 simulations. Section 4 presents the results of diagnostic experiments with the QTCM. Section 5 consists of a summary and discussion.

2. Datasets, model and methodology

2.1 Datasets

We use monthly diagnostic surface temperature from NOAA NCEP-NCAR CDAS-1 (Kalnay et al. 1996) to compute the Niño-3.4 SST index (Trenberth 1997). Meteorological variables including sea level pressure, air temperature, sea surface temperature, and precipitation are taken from NCEP-NCAR reanalysis (Kalnay et al. 1996) and AMIP runs using prescribed SST anomalies for the period 1980-2001 of several models participating in CMIP5 (Taylor et al. 2012). For presentation, we only show results from five atmospheric general circulation models (AGCMs): GFDL HIRAM C360, CCSM4, CanAM4, GISS, and HadGEM2.

2.2 The QTCM

The QTCM belongs in a class of tropical atmospheric models of intermediate complexity that occupies a niche between GCMs and simple models. The model takes analytical solutions that hold approximately under quasi-equilibrium (QE) conditions and employs them as leading basis functions to represent the vertical structure of the flow. The primitive equations are then projected onto these simplified vertical structures, with self-consistent nonlinear terms retained in advection, moist convection, and vertical momentum transfer terms, among others. A more detailed model description can be found in Neelin and Zeng (2000). The present study uses QTCM1, version 2.3, which retains a single basis function for the vertical structure of temperature, and two basis functions for velocity, i.e., the baroclinic and barotropic modes. This and related QTCM versions have been used to analyze the moist dynamics of ENSO teleconnections in a number of contexts (Su et al. 2001; Su et al. 2003; Su et al. 2005; Neelin and Su 2005; Lintner and Chiang 2007).

The QTCM is a useful tool to analyze the contributions of baroclinic and barotropic modes to the ENSO tropical teleconnections. In the model, temperature anomalies directly force a baroclinic response, and barotropic motion is then excited through the interactions with baroclinic motion. The equation for the barotropic stream function ψ_0 is:

$$\begin{aligned}&\partial_t \nabla^2 \psi_0 + curl_z(\mathbf{v}_0 \cdot \nabla \mathbf{v}_0) - K_H \nabla^4 \psi_0 + \beta v_0 \\ &= -curl_z(\left\langle V_1^2 \right\rangle \mathbf{v_1} \cdot \nabla \mathbf{v_1}) - curl_z(\left\langle V_1^2 \right\rangle (\nabla \cdot \mathbf{v_1}) \mathbf{v_1}) - curl_z(\varepsilon_0 \mathbf{v_0} + \varepsilon_{10} \mathbf{v_1})\end{aligned} \quad (1)$$

The terms on the right hand side of (1) act as an effective Rossby wave source, which acts to excite the barotropic mode in a manner akin to well-known studies of barotropic teleconnections (Hoskins and Karoly 1981; Held and Kang 1987; Sardeshmukh and Hoskins 1988). We remark, first, that this is not quite the same as the Rossby wave source that would be defined by assuming an upper-level forcing applied to the barotropic mode, but rather results from a representation of the modal breakdown over the full depth of the troposphere (Neelin and Zeng 2000; Majda and Biello 2003). Under certain circumstances, in particular if one could assume horizontally constant vertical shear in the geostrophic approximation, an alternate vertical mode decomposition can be constructed in which the barotropic mode properties are modified to create an external or equivalent barotropic mode with some baroclinic component included (Held et al. 1985). The interaction term approach here treats the same process in a manner that is easier to use in a spatially varying basic state. Second, the third term on the right hand side is shown in a form where it is proportional to surface stress, which can be simpler for diagnosis and interpretation. However it might alternately be separated into a forcing term $-curl_z(\varepsilon_{10}\mathbf{v}_1)$, with the $-curl_z(\varepsilon_0\mathbf{v}_0)$ portion on the left hand side. Interpreting the respective terms in the effective Rossby wave source in (1), the sources of baroclinic-barotropic interaction are: 1) $-curl_z(\langle V_1^2\rangle \mathbf{v_1}\cdot\nabla\mathbf{v_1})$, representing interactions of vertical shear in horizontal advection terms; 2) $-curl_z(\langle V_1^2\rangle(\nabla\cdot\mathbf{v_1})\mathbf{v_1})$, representing vertical motion advecting the baroclinic wind component; and 3) $-curl_z(\varepsilon_0\mathbf{v}_0+\varepsilon_{10}\mathbf{v}_1)$, representing interactions via surface stress in the boundary layer. Ji et al. (2014) analyzed the effects of each mechanism on forcing barotropic mode and associated teleconnection pathways from a tropical heat source.

2.3 Methodology

In this subsection we describe the method applied to separate the baroclinic and barotropic components of SLP in both reanalysis data and AGCM model outputs. The hydrostatic equation in pressure coordinates is: $\partial_p\phi = -RT/p$. Taking a vertical integral of the equation yields $\phi = \int_p^{p_r} RT\, d\ln p + \phi_r$, where p_r is a reference pressure and ϕ_r is the geopotential on that pressure surface. The momentum equations combined with the hydrostatic equation can be written as,

$$\begin{aligned}&(\partial_t + \mathbf{v}\cdot\nabla + \omega\partial_p - K_H\nabla^2)\mathbf{v} + f\mathbf{k}\times\mathbf{v} + g\partial_p\tau \\ &= -\nabla\int_p^{p_r} RT\, d\ln p - \nabla\phi_r\end{aligned} \qquad (2)$$

where K_H is the horizontal diffusion coefficient, τ is vertical flux of horizontal momentum, and g is gravitational acceleration.

The vertical average over the troposphere is defined as $\hat{X} = \langle X\rangle = p_T^{-1}\int_{p_{rt}}^{p_{rs}} X\, dp$, where p_{rs} and p_{rt} are pressure at the near-surface and tropopause reference levels, respectively, and $p_T = p_{rs} - p_{rt}$. We define the surface geopotential as $\phi_s = \phi_{s1} + \phi_{s0}$, with $\phi_{s0} = \langle\phi\rangle$, and $\phi_{s1} = \phi_s - \phi_{s0} \approx \phi_{1000} - \langle\phi\rangle$. Assuming that density is constant between the surface and the reference level, the baroclinic and barotropic components of the surface pressure are then:

$$p_s = \rho\phi_{s0} + \rho\phi_{s1} \tag{3}$$

We note that neglecting advection by baroclinic wind and surface drag on the baroclinic mode, the baroclinic mode and barotropic mode will be separable. The solution of (2) must simply match the vertical structures of the barotropic and baroclinic pressure gradient terms.

The separation of SLP into baroclinic and barotropic components in the QTCM is straightforward. Firstly, the baroclinic and barotropic components of surface geopotential are calculated from integration of the baroclinic temperature and barotropic momentum equation respectively. Secondly, the baroclinic and barotropic SLP components are obtained by multiplying the corresponding components of surface geopotential by the near surface air density.

We perform several diagnosis experiments with the QTCM to analyze the pathway for the atmospheric response in the tropical western Pacific associated with ENSO. In these experiments, the interannual variations in the baroclinic-barotropic interaction terms are suppressed by replacing these terms with their monthly mean values from a 100-year climatological model run. To gain insight on the geographical extent of the region where the interactions act in the tropical teleconnections, interannual variations are suppressed over increasingly wider latitudinal bands in the tropical Pacific.

3. Baroclinic and barotropic modes in ENSO tropical teleconnections

In this section, we examine the meteorological anomalies associated with ENSO. These are defined by regression of each quantity onto the Niño-3.4 SST index. We start with the monthly means for winter season (December, January and February) in the NCEP-NCAR reanalysis. The results are shown in the panels of Fig. 1, which show good agreement with previous observational results, notably, Wallace et al. (1998), which helped inspire the investigation here.

Figure 1a SST shows positive anomalies in the central and eastern equatorial Pacific. Figure 1b shows positive precipitation anomalies around the central equatorial Pacific with negative anomalies around them and maximum values slightly to the west of the largest SST anomalies. The SLP anomalies (Fig. 1c) are reminiscent of the classic Southern Oscillation pattern: strong negative and positive anomalies in the eastern and western Pacific, respectively. The anomalies in vertical mean temperature throughout the troposphere (Fig.1d) shows positive values over a broad region of the tropical central and eastern Pacific. The structure of these temperature anomalies is consistent with a baroclinic Rossby wave straddling the equator to the west and a Kelvin wave around the equator to the east of the precipitation anomalies in Fig. 1b, which correspond to regions of deep convective heating anomalies. The magnitude of the tropospheric temperature anomalies drops off sharply from around the dateline towards the western Pacific. Thus, the SLP anomalies in this region are well separated from the baroclinic signal associated with the temperature anomalies.

Next, we break down the SLP anomalies in Fig. 1c into their baroclinic and barotropic components. The baroclinic component (Fig. 2a) has strong magnitudes in the eastern Pacific in the same region where tropospheric temperature anomalies are strong (Fig. 1d), as expected from the hydrostatic relationship. The barotropic component (Fig. 2b), on the other hand, shows a broad band of anomalies across the entire tropics with a clear local maximum in the western Pacific, where the values is comparable to those of the total SLP anomalies in Fig. 1c.

To examine whether the anomalies in SLP and its baroclinic and barotropic components, as well as in tropospheric temperatures strongly depend on the seasonal cycle, we recompute the corresponding figures by using the monthly mean fields for the 20-year (1982-2001) period from the NCEP-NCAR reanalysis. The results are shown in Fig. 3. Similar patterns are obtained, albeit with weaker magnitudes in the annual case. This suggests that the spatial discrepancy between regions of larger SLP anomalies and tropospheric temperature anomalies associated with ENSO in the tropical Pacific is robust throughout the year, despite the seasonal asymmetries of the subtropical circulation and associated baroclinic and barotropic interactions in the subtropics.

It is also useful to have an estimate of how the teleconnection pattern translates into surface wind. Figures s1a and s2a show the regression of NCEP-NCAR reanalysis surface zonal wind and vector surface wind onto Niño3.4, respectively. Figures s1b and s2b show the reconstructed winds from the NCEP 1000mb geopotential field using simple damping assumptions (Stevens et al. 2002). The reconstruction compares to the actual surface winds sufficiently well over oceans to motivate reconstructing separately the baroclinic and barotropic components from the respective geopotential contributions. In Figs. s1c, d, the baroclinic zonal wind contribution near the equator in the tropical Pacific is substantially larger than the barotropic contribution, so an approximation that would include only the baroclinic mode would have qualitatively useful features. However, the barotropic contribution is not negligible even in the deep tropics. Furthermore, in the subtropics, the barotropic contribution considerably cancels the baroclinic contribution to the surface wind, as one would expect when surface drag is effective at reducing the near-surface wind.

In Fig. 4, we further decompose the baroclinic component of SLP into its free troposphere (900hpa-150hpa) contribution (Fig. 4a) and boundary layer (1000hpa-900hpa) contribution (Fig. 4b). The corresponding decomposition of the tropospheric temperature anomalies, i.e., the vertical average over free troposphere and boundary layer are also shown in Figs 4c and 4d. The tropospheric temperature anomalies in the free troposphere and the boundary layer have similar magnitudes but very different patterns, with the latter resembling the SST anomalies in Fig. 1a. On the contrary, the baroclinic contribution to SLP anomalies in the free troposphere is much larger than in the boundary layer. Notice that in either case, the contributions to SLP anomalies in the western Pacific are very weak.

In the following, we examine the anomalies in SLP and tropospheric temperature associated with ENSO in the AGCM simulations described in section 2 using the monthly mean fields for the 20-year (1982-2001) period. Figure 5 shows the SLP anomalies, the baroclinic and barotropic components of these anomalies, and the tropospheric temperature anomalies associated with ENSO based on the GFDL HiRAM-

C360. The results obtained with the NCEP-NCAR reanalysis (Fig. 3) and the GFDL HiRAM-C360 (Fig. 5) are very similar, both in patterns and magnitudes. In particular, the positive SLP anomalies in the western Pacific are due to the barotropic contribution since the baroclinic one has the opposite sign and is not statistically significant. We show in Fig. 6 the SLP and the tropospheric temperature anomalies based on four other models participating in the CMIP5, which are all consistent with the corresponding patterns in the NCEP NCAR reanalysis (Fig. 3). The large SLP anomalies and weak tropospheric temperature anomalies in the western Pacific are also present in the AGCMs of other CMIP5 models (not shown). For a more quantitative assessment of the similarity between the anomaly patterns in the models and the NCEP-NCAR reanalysis, we calculate the spatial correlation between the corresponding anomalous patterns of SLP and tropospheric temperature in model and reanalysis over the area ranging from 90°E to 60°W and 30°N to 30°S. The correlations are high for all 30 models (>0.90). The only exception is the tropospheric temperature pattern in HADGEM2-A (Fig. 6h), which has a correlation of slightly lower than 0.90 with the NCEP-NCAR data. In this model, the temperature anomalies in the Indian Ocean and Africa region are weaker than those from the NCEP-NCAR reanalysis and other CMIP5 models.

4. Diagnosis experiment with the QTCM

In this section, we use the QTCM to gain insight into the dynamical mechanisms at work for the ENSO tropical teleconnection process. The question to be addressed is how the barotropic teleconnection patterns are forced in the western Pacific by the effective barotropic Rossby wave source due to the baroclinic-barotropic interactions?

Figure 7 shows the wintertime (December, January and February) meteorological anomalies associated with ENSO based on a 20-year (1982-2001) QTCM run with observed SSTs. A comparison between panels in Fig. 7 with those obtained using the NCEP-NCAR reanalysis in Figs. 1 and 2, reveal similarities of pattern but weaker amplitudes in the simulation. The corresponding annual regression analysis from the QTCM simulations is shown in supplementary Fig. s3.

Figure 8 displays the December-February mean SLP differences between two 100-year QTCM simulations: one with monthly composites of ENSO SST anomalies and the other with monthly-mean climatological SSTs. In Fig 8a, the SLP anomalies shows a similar pattern to the one obtained by regressing SLP onto Niño-3.4 SST shown in Fig. 7a. Note that the regression plots in Fig. 7 show values per degree of SST anomalies associated with ENSO, whereas the fields in Figs. 8 are associated with SST anomalies in the order of 2-3 K, Thus, values in Fig. 7 are all 2-3 times smaller than those in Fig 8. The breakdown of the SLP anomalies in Fig. 8a into barotropic and baroclinic components is shown in Fig. s4, which can be compared with Figs. 7b and 7c, respectively. As we can see, the positive SLP anomalies in the western Pacific, especially the maximum around 180°, 20°N, are due to the barotropic contribution. Figures 8b, 8c, and 8d portray the impact of suppressing the Rossby wave source in the region from 150°E to 100°W for successively wider latitudinal bands around the equator. Comparisons among Figs. 8b, 8c, and 8d, reveal that the SLP anomalies in the western Pacific are gradually weaker with wider bands. This weakening indicates that the baroclinic-barotropic interactions in the Pacific subtropics are important in addition to those in the tropics to the SLP anomalies in the western Pacific. For reference, Fig s5 presents the total Rossby wave source as well as its three components (shear advection, surface drag and vertical advection) between the two 100-year simulations. The shear advection in the subtropics (Fig. s5b) that occurs as the horizontal advection term, arising substantially from the baroclinic anomalies interacting with basic state vertical shear, seems to comprise a significant part of the subtropical effective Rossby wave source (Fig. s5a). Although in the QTCM experiment, we suppress the surface stress term as a whole, Fig. s5c shows only the baroclinic portion $-curl_z(\varepsilon_{10}\mathbf{v}_1)$ as forcing component in the surface drag, since the barotropic portion $-curl_z(\varepsilon_0\mathbf{v}_0)$ acts as damping on the barotropic mode. Figure 8e shows the SLP difference with suppressed Rossby wave source in a tropical band from 25°N to 25°S. If Fig. 8e is compared to Fig. 8c, the subtropical edges show some small-scale, wavelike features in Fig. 8e, but the western Pacific is not very different between the two panels. Thus, the baroclinic-barotropic interactions in the tropics outside the Pacific will affect baroclinic processes in the subtropics, but do not have a significant effect on the western Pacific SLP anomaly pattern.

5. Conclusions

We have investigated the mechanisms that generate the SLP anomalies in the western Pacific, which have long been known as part of the classic Southern Oscillation pattern associated with ENSO. Contrary to traditional studies that assume a single deep baroclinic mode for ENSO response in the tropics, the SLP anomalies in the western Pacific are spatially well separated from the baroclinic signal associated with the tropospheric temperature anomalies in NCEP-NCAR reanalysis, CMIP5 models, and QTCM. Separation of the SLP into its baroclinic and barotropic components indicates that the baroclinic mode SLP contributions extend over the central and eastern equatorial Pacific, coincident with the temperature anomalies, and in a spatial pattern consistent with first baroclinic mode wave dynamics. On the other hand, SLP anomalies in the western Pacific arise primarily from barotropic mode contributions, and thus must be associated with a slightly more complex dynamical pathway.

The following pathway is found in QTCM diagnostic experiments: interactions with SST anomalies create the baroclinic mode signal in the central and Eastern Pacific, but baroclinic-barotropic interactions, arising substantially in the subtropical Pacific, create a barotropic response that yields the SLP anomaly pattern in the western Pacific. In a set of QTCM experiments, we suppress anomalies in baroclinic-barotropic interaction terms over increasingly wider latitudinal bands in the tropical Pacific, to diagnose their effects on the SLP anomalies in the western Pacific associated with ENSO. In the 15°N-15°S experiment, the pressure signals in the western Pacific are only partly suppressed, whereas in the 30°N-30°S suppression experiment, the anomalies in the western Pacific are almost entirely removed. We note that the suppression experiment does not necessarily imply that the westward teleconnection is purely barotropic. However it does demonstrate that anomalies of an effective barotropic Rossby wave source due to the baroclinic-barotropic interaction terms are key to maintaining the largely barotropic signal in the Western Pacific that yields the classical SLP patterns in this region.

Furthermore, it demonstrates the importance of the subtropical contribution to this effective Rossby wave source, arising substantially from the vertical shear term that occurs as baroclinic anomalies interact with basic state vertical shear approaching the subtropical jet.

Acknowledgments

We thank Joyce Meyerson for assistance with graphics. This work was supported in part by National Science Foundation grants AGS-1102838 and AGS-1041477, National Oceanic and Atmospheric Administration grants NA11OAR4310099 and NA14OAR4310274, and a scholarship awarded by the Chinese Scholarship Council to support XJ's PhD study at University of California, Los Angeles. We thank Hui Su and Matt Munnich for unpublished initial QTCM and NCEP analysis (2004) related to this problem. We also thank Xin Qu for his comments. JDN would like to acknowledge the role of Wallace et al. (1998) Plate 8 in which the mismatch of SLP and tropospheric temperature patterns led to the puzzle analyzed here.

References:

Bacmeister, J. T., and M. J. Suarez, 2002: Wind stress simulations and the equatorial momentum budget in an AGCM. *J Atmos Sci*, **59,** 3051-3073.

Biello, J. A., and A. J. Majda, 2004a: Boundary layer dissipation and the nonlinear interaction of equatorial baroclinic and barotropic Rossby waves. *Geophys Astro Fluid*, **98,** 85-127.

Biello, J. A., and A. J. Majda, 2004b: The effect of meridional and vertical shear on the interaction of equatorial baroclinic and barotropic Rossby waves. *Stud Appl Math*, **112,** 341-390.

Branstator, G., 1983: Horizontal Energy Propagation in a Barotropic Atmosphere with Meridional and Zonal Structure. *J Atmos Sci*, **40,** 1689-1708.

Chiang, J. C. H., and A. H. Sobel, 2002: Tropical tropospheric temperature variations caused by ENSO and their influence on the remote tropical climate. *J Climate*, **15,** 2616-2631.

Gill, A. E., 1980: Some Simple Solutions for Heat-Induced Tropical Circulation. *Q J Roy Meteor Soc*, **106,** 447-462.

Held, I. M., and I. S. Kang, 1987: Barotropic Models of the Extratropical Response to El-Nino. *J Atmos Sci*, **44,** 3576-3586.

Held, I. M., R. L. Panetta, and R. T. Pierrehumbert, 1985: Stationary External Rossby Waves in Vertical Shear. *J Atmos Sci*, **42**, 865-883.

Horel, J. D., and J. M. Wallace, 1981: Planetary-Scale Atmospheric Phenomena Associated with the Southern Oscillation. *Mon Weather Rev*, **109,** 813-829.

Hoskins, B. J., and D. J. Karoly, 1981: The Steady Linear Response of a Spherical Atmosphere to Thermal and Orographic Forcing. *J Atmos Sci*, **38,** 1179-1196.

Ji, X., J. D. Neelin, S. K. Lee, and C. R. Mechoso, 2014: Interhemispheric Teleconnections from Tropical Heat Sources in Intermediate and Simple Models. *J Climate*, **27,** 684-697.

Kalnay, E., and Coauthors, 1996: The NCEP/NCAR 40-year reanalysis project. *B Am Meteorol Soc*, **77,** 437-471.

Kiladis, G. N., and H. F. Diaz, 1989: Global Climatic Anomalies Associated with Extremes in the Southern Oscillation. *J Climate*, **2,** 1069-1090.

Kumar, A., and M. P. Hoerling, 2003: The nature and causes for the delayed atmospheric response to El Nino. *J Climate*, **16,** 1391-1403.

Lee, S. K., C. Z. Wang, and B. E. Mapes, 2009: A Simple Atmospheric Model of the Local and Teleconnection Responses to Tropical Heating Anomalies. *J Climate*, **22,** 272-284.

Lintner, B. R., and J. C. H. Chiang, 2007: Adjustment of the remote tropical climate to El Nino conditions. J Climate, **20**, 2544-2557.

Majda, A. J., and J. A. Biello, 2003: The nonlinear interaction of barotropic and equatorial baroclinic Rossby waves. *J Atmos Sci*, **60,** 1809-1821.

Neelin, J. D., and N. Zeng, 2000: A quasi-equilibrium tropical circulation model - Formulation. *J Atmos Sci*, **57,** 1741-1766.

Neelin, J. D. and H. Su, 2005: Moist teleconnection mechanisms for the tropical South American and Atlantic sector. *J. Climate*, **18**, 3928-3950.

Sardeshmukh, P. D., and B. J. Hoskins, 1988: The Generation of Global Rotational Flow by Steady Idealized Tropical Divergence. *J Atmos Sci*, **45,** 1228-1251.

Simmons, A. J., 1982: The Forcing of Stationary Wave Motion by Tropical Diabatic Heating. *Q J Roy Meteor Soc*, **108,** 503-534.

Simmons, A. J., J. M. Wallace, and G. W. Branstator, 1983: Barotropic Wave-Propagation and Instability, and Atmospheric Teleconnection Patterns. *J Atmos Sci*, **40,** 1363-1392.

Stevens, B., J. J. Duan, J. C. McWilliams, M. Munnich, and J. D. Neelin, 2002: Entrainment, Rayleigh friction, and boundary layer winds over the tropical Pacific. *J Climate*, **15,** 30-44.

Su, H., and J. D. Neelin, 2002: Teleconnection mechanisms for tropical Pacific descent anomalies during El Nino. *J Atmos Sci*, **59,** 2694-2712.

Su, H., J. D. Neelin, and C. Chou, 2001: Tropical teleconnection and local response to SST anomalies during the 1997-1998 El Nino. *J Geophys Res-Atmos*, **106,** 20025-20043.

Su, H., J. D. Neelin, and J. E. Meyerson, 2003: Sensitivity of tropical tropospheric temperature to sea surface temperature forcing. *J. Climate*, 16, 1283-1301.

Su, H., J. D. Neelin and J. E. Meyerson, 2005: Mechanisms for Lagged Atmospheric Response to ENSO SST Forcing. *J. Climate*, **18**, 4195-4215.

Taylor, K. E., R. J. Stouffer, and G. A. Meehl, 2012: An Overview of Cmip5 and the Experiment Design. *B Am Meteorol Soc*, **93,** 485-498.

Trenberth, K. E., 1997: The definition of El Nino. *B Am Meteorol Soc*, **78,** 2771-2777.

Wallace, J. M., E. M. Rasmusson, T. P. Mitchell, V. E. Kousky, E. S. Sarachik, and H. von Storch, 1998: The structure and evolution of ENSO-related climate variability in the tropical Pacific: Lessons from TOGA. *J Geophys Res-Oceans*, **103,** 14241-14259.

Wang, B., and X. S. Xie, 1996: Low-frequency equatorial waves in vertically sheared zonal flow .1. Stable waves. *J Atmos Sci*, **53,** 449-467.

Webster, P. J., 1972: Response of Tropical Atmosphere to Local, Steady Forcing. *Mon Weather Rev*, **100,** 518-&.

Figure captions:

Fig. 1 a) SST (K °C^{-1}), b) precipitation (mm day^{-1} °C^{-1}), c) SLP (Pa °C^{-1}), and d) tropospheric temperature (K °C^{-1}) from NCEP-NCAR reanalysis DJF regression onto Niño3.4, with a two-tailed *t* test applied to the regression values and stippled at 99% confidence.

Fig. 2 a) SLP baroclinic component (Pa °C-1) and b) SLP barotropic component (Pa °C-1) from NCEP-NCAR reanalysis DJF regression onto Niño3.4, with a two-tailed t test applied to the regression values and stippled at 99% confidence.

Fig. 3 a) SLP (Pa °C^{-1}), b) SLP baroclinic component (Pa °C^{-1}), c) SLP barotropic component (Pa °C^{-1}), and d) tropospheric temperature (K °C^{-1}) from NCEP-NCAR reanalysis *annual* regression onto Niño3.4, with a two-tailed *t* test applied to the regression values and stippled at 99% confidence.

Fig. 4 a) SLP baroclinic free troposphere component (Pa °C^{-1}), b) SLP baroclinic boundary layer component (Pa °C^{-1}), c) tropospheric temperature average over free troposphere (K °C^{-1}), and d) tropospheric temperature average over boundary layer (K °C^{-1}) from NCEP-NCAR reanalysis *annual* regression onto Niño3.4, with a two-tailed *t* test applied to the regression values and stippled at 99% confidence.

Fig. 5 a) SLP (Pa °C^{-1}), b) SLP baroclinic component (Pa °C^{-1}), c) SLP barotropic component (Pa °C^{-1}), and d) tropospheric temperature (K °C^{-1}) from GFDL HIRAM C360 run with prescribed SSTs *annual* regression onto Niño3.4, with a two-tailed *t* test applied to the regression values and stippled at 99% confidence. Note in b), c), and d), land points for which temperature does not extend to 1000 mbar are masked; SLP interpolation in a) is as provided by the modeling center.

Fig. 6 a) c) e) and g) SLP (Pa °C^{-1}), b) d) f) and h) tropospheric temperature (K °C^{-1}) from selected AGCM runs participating in CMIP5 *annual* regression onto Niño3.4, with a two-tailed *t* test applied to the regression values and stippled at 99% confidence.

Fig. 7 a) SLP (Pa °C^{-1}), b) SLP baroclinic component (Pa °C^{-1}), c) SLP barotropic component (Pa °C^{-1}), d) tropospheric temperature (K °C^{-1}), and e) precipitation (mmday^{-1} °C^{-1}) from a 20yr QTCM run with real-time SSTs DJF regression onto Niño3.4, with a two-tailed *t* test applied to the regression values and stippled at 99% confidence.

Fig. 8 SLP anomalies (Pa) associated with ENSO from QTCM experiments with suppressed barotropic Rossby wave source. a) Control run, vs. Rossby wave source suppressed over b) 150°E-100°W, 15°N-15°S, c) 150°E-100°W, 25°N-25°S, d) 150°E-100°W, 30°N-30°S, and e) 0-360°, 25°N-25°S, stippled where a *t* test yields grid points significant at or above the 99% confidence level.

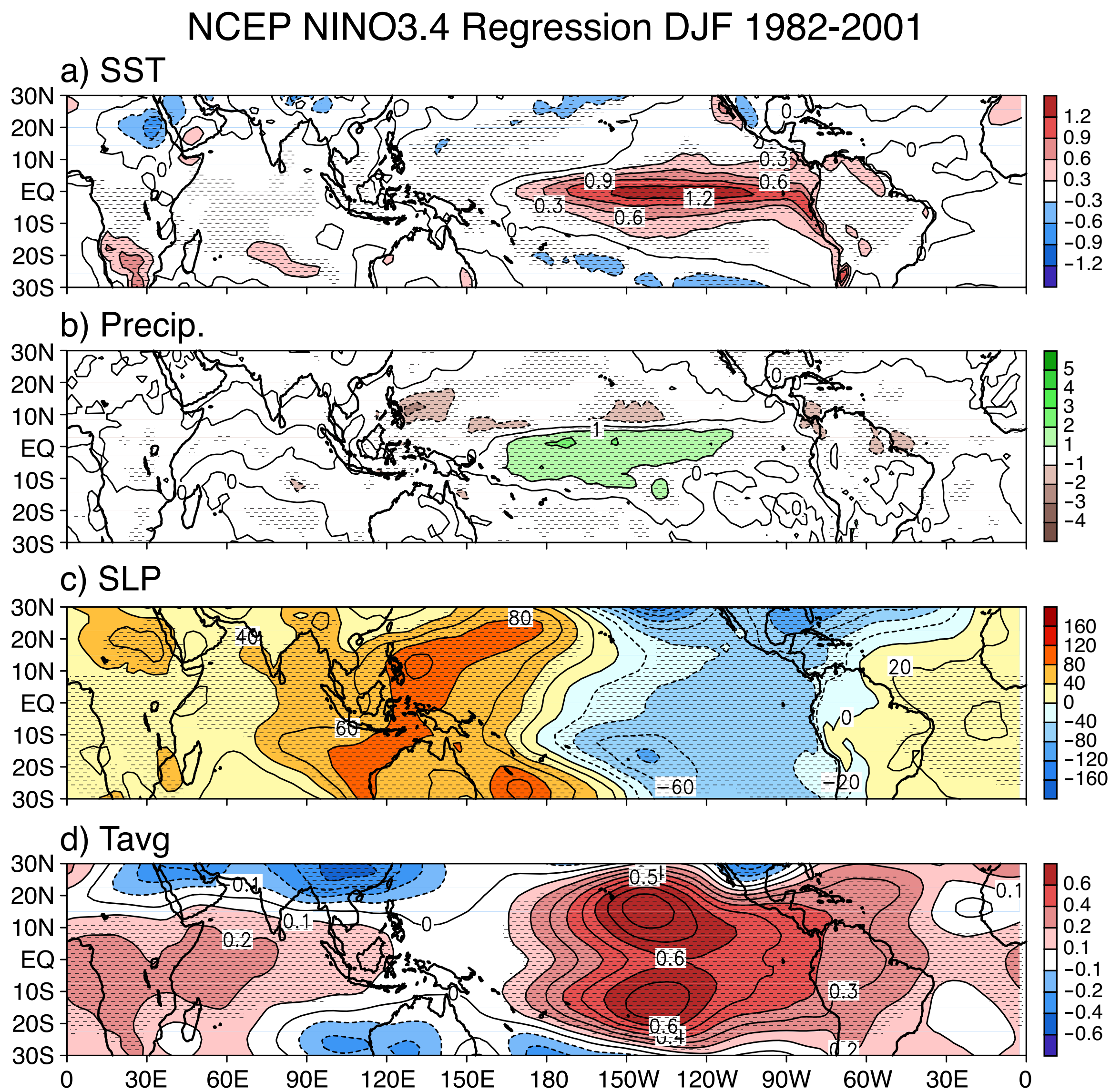

Fig. 1 a) SST (K °C^{-1}), b) precipitation (mm day^{-1} °C^{-1}), c) SLP (Pa °C^{-1}), and d) tropospheric temperature (K °C^{-1}) from NCEP-NCAR reanalysis DJF regression onto Niño3.4, with a two-tailed *t* test applied to the regression values and stippled at 99% confidence.

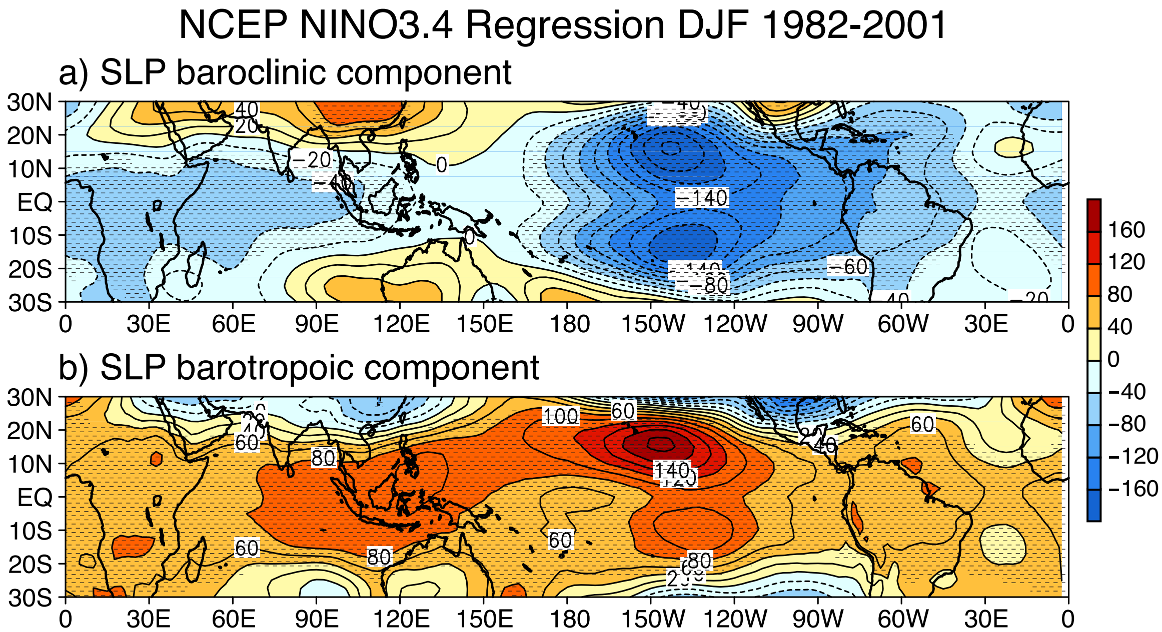

Fig. 2 a) SLP baroclinic component (Pa °C^{-1}) and b) SLP barotropic component (Pa °C^{-1}) from NCEP-NCAR reanalysis DJF regression onto Niño3.4, with a two-tailed *t* test applied to the regression values and stippled at 99% confidence.

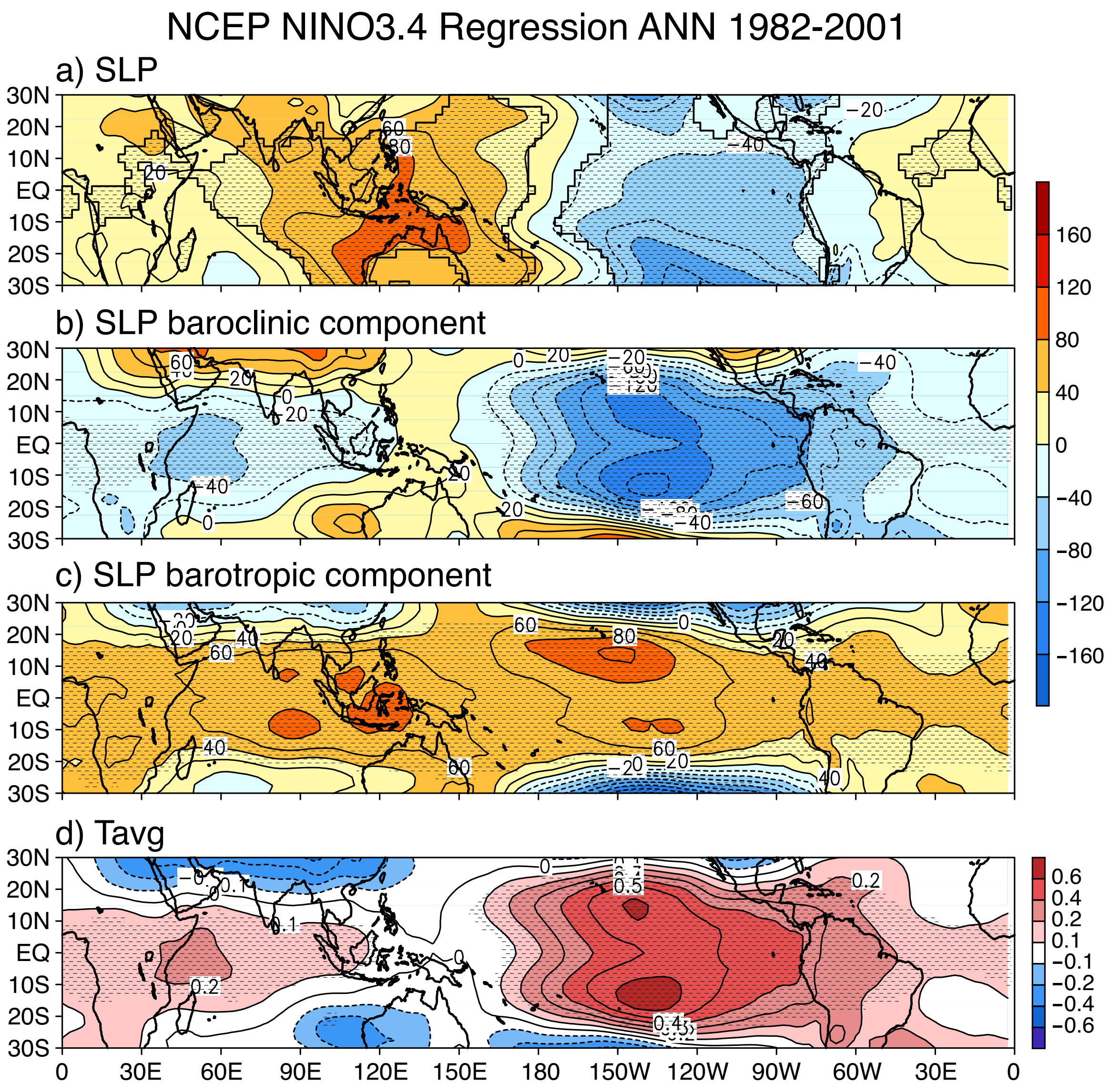

Fig. 3 a) SLP (Pa °C^{-1}), b) SLP baroclinic component (Pa °C^{-1}), c) SLP barotropic component (Pa °C^{-1}), and d) tropospheric temperature (K °C^{-1}) from NCEP-NCAR reanalysis *annual* regression onto Niño3.4, with a two-tailed *t* test applied to the regression values and stippled at 99% confidence.

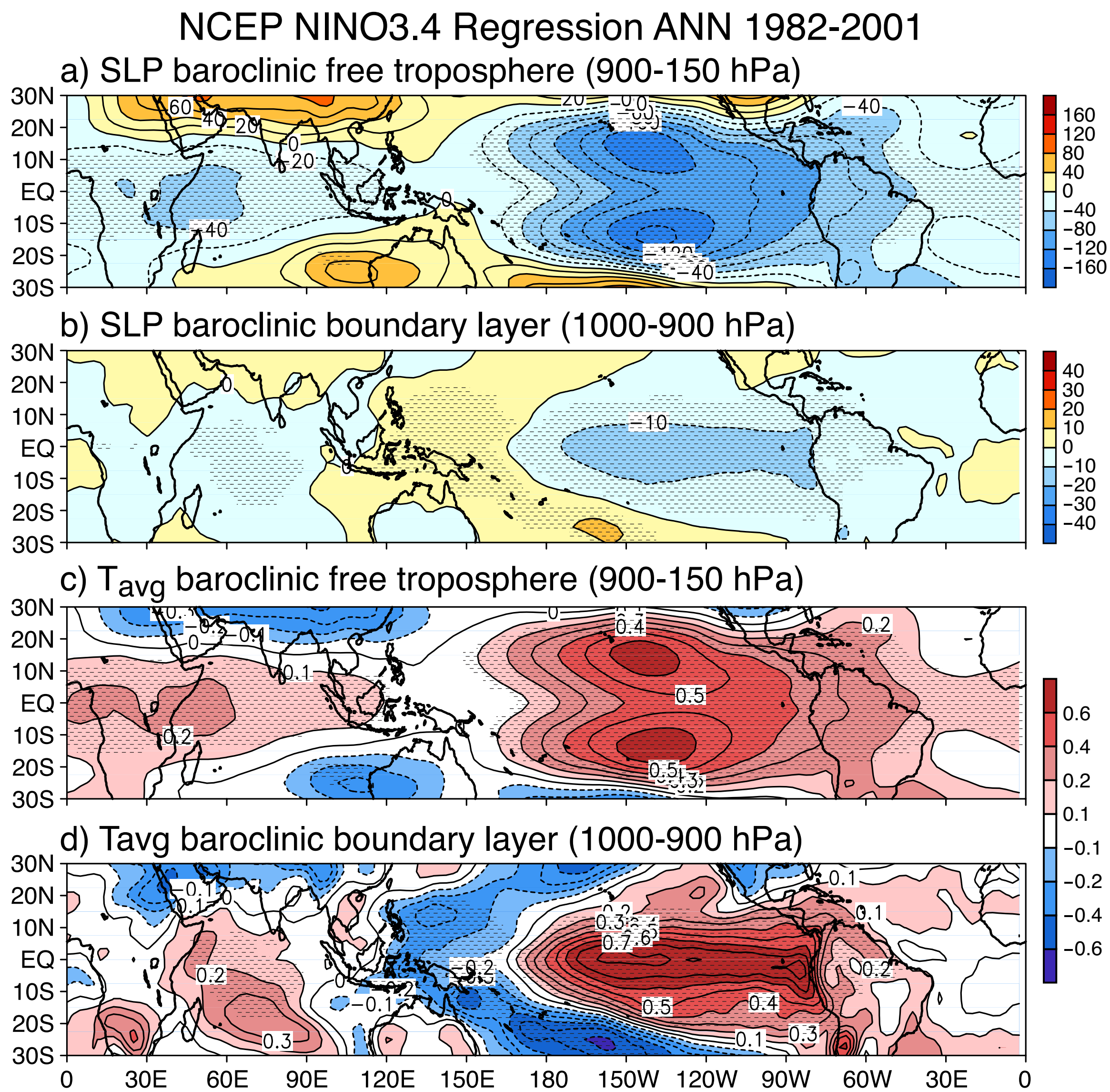

Fig. 4 a) SLP baroclinic free troposphere component (Pa °C^{-1}), b) SLP baroclinic boundary layer component (Pa °C^{-1}), c) tropospheric temperature average over free troposphere (K °C^{-1}), and d) tropospheric temperature average over boundary layer (K °C^{-1}) from NCEP-NCAR reanalysis *annual* regression onto Niño3.4, with a two-tailed *t* test applied to the regression values and stippled at 99% confidence.

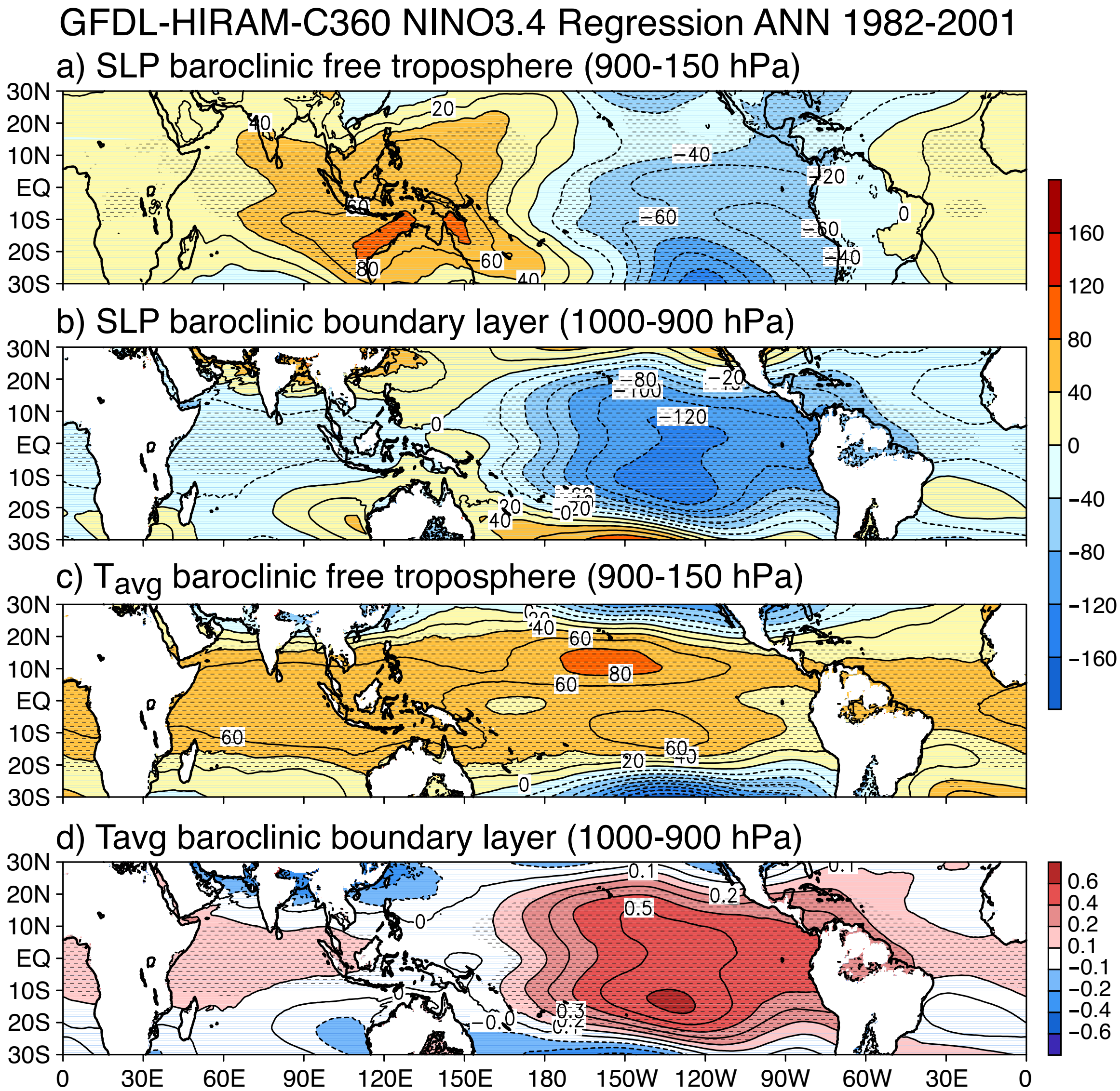

Fig. 5 a) SLP (Pa °C^{-1}), b) SLP baroclinic component (Pa °C^{-1}), c) SLP barotropic component (Pa °C^{-1}), and d) tropospheric temperature (K °C^{-1}) from GFDL HIRAM C360 run with prescribed SSTs *annual* regression onto Niño3.4, with a two-tailed *t* test applied to the regression values and stippled at 99% confidence. Note in b), c), and d), land points for which temperature does not extend to 1000 mbar are masked; SLP interpolation in a) is as provided by the modeling center.

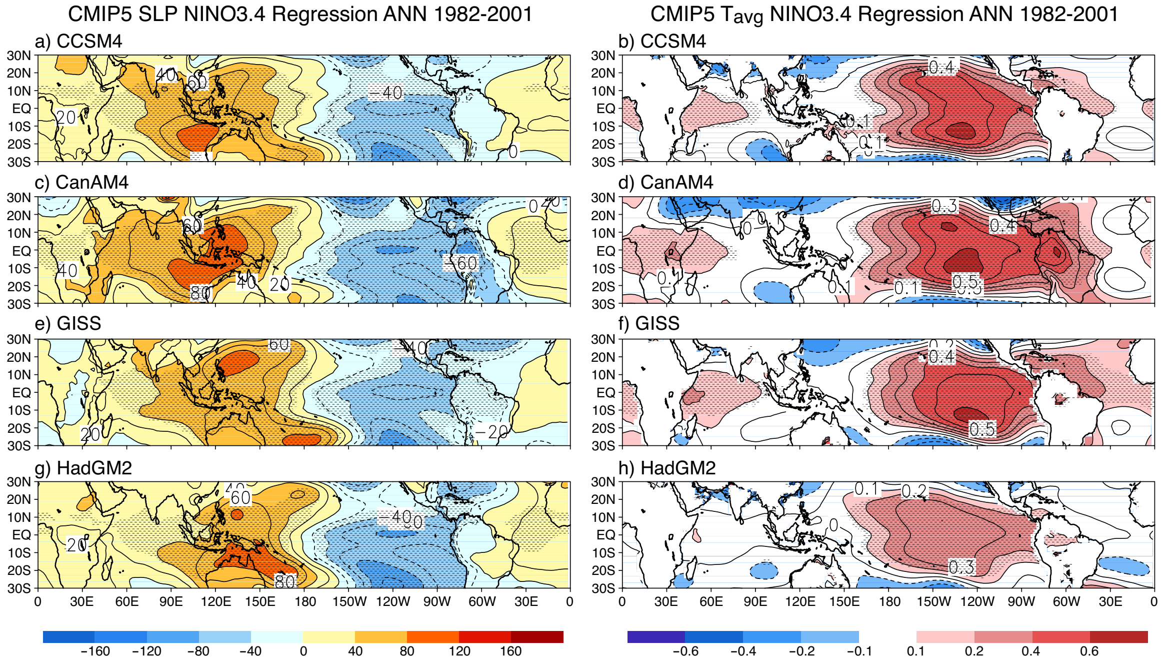

Fig. 6 a) c) e) and g) SLP (Pa °C^{-1}), b) d) f) and h) tropospheric temperature (K °C^{-1}) from selected AGCM runs participating in CMIP5 *annual* regression onto Niño3.4, with a two-tailed *t* test applied to the regression values and stippled at 99% confidence.

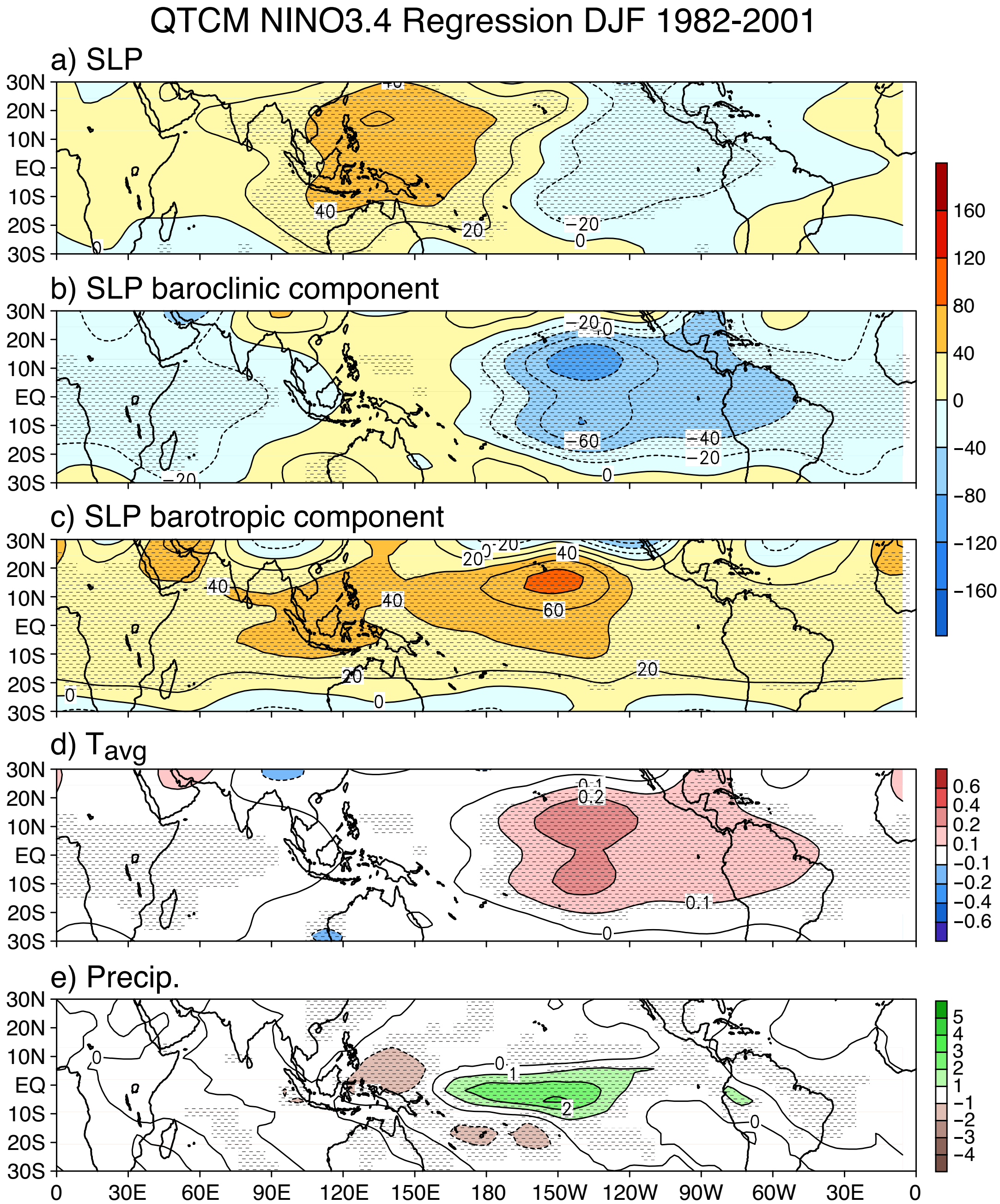

Fig. 7 a) SLP (Pa °C^{-1}), b) SLP baroclinic component (Pa °C^{-1}), c) SLP barotropic component (Pa °C^{-1}), d) tropospheric temperature (K °C^{-1}), and e) precipitation (mmday^{-1} °C^{-1}) from a 20yr QTCM run with real-time SSTs DJF regression onto Niño3.4, with a two-tailed t test applied to the regression values and stippled at 99% confidence.

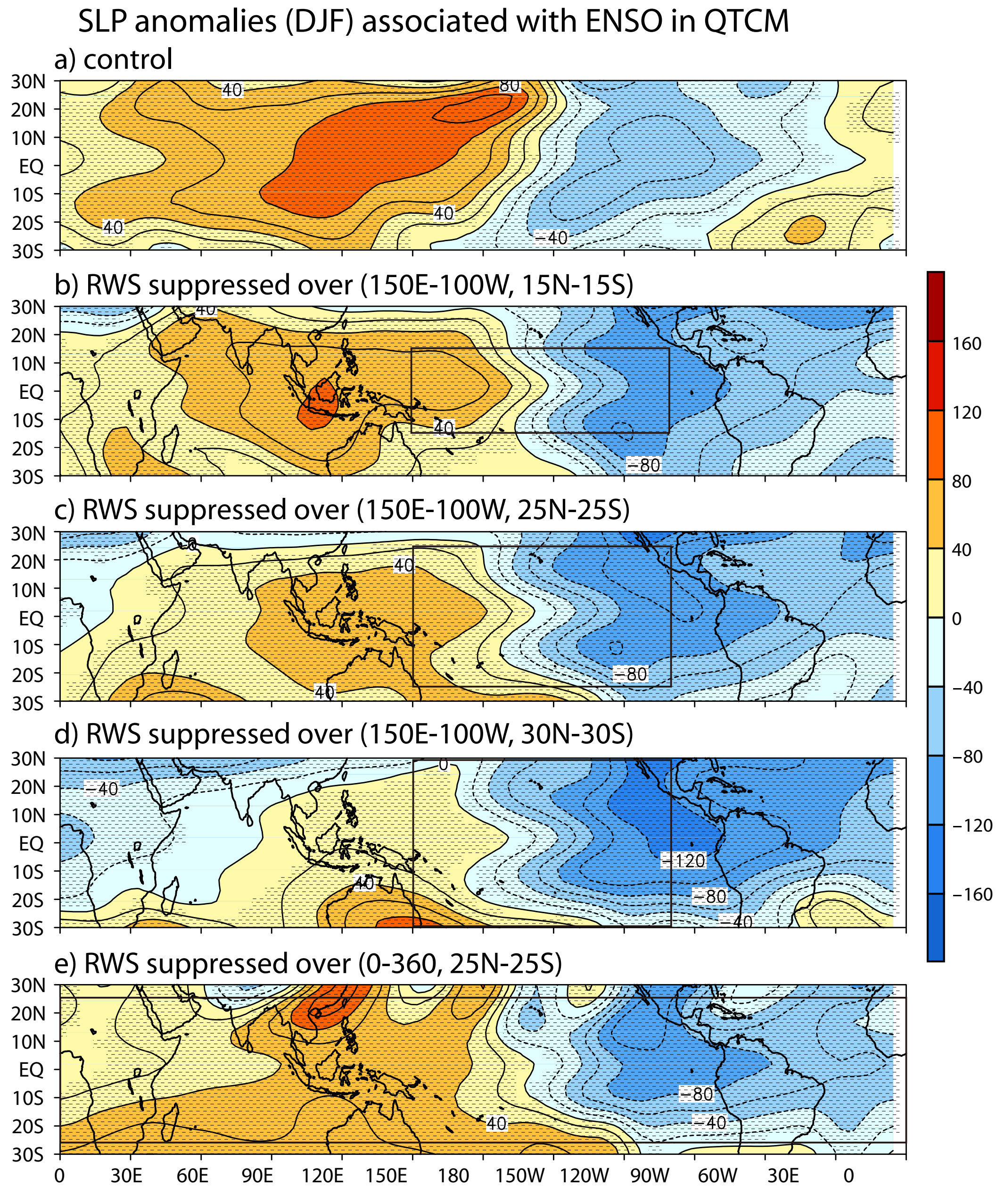

Fig. 8 SLP anomalies (Pa) associated with ENSO from QTCM experiments with suppressed barotropic Rossby wave source. a) Control run, vs. Rossby wave source suppressed over b) 150°E-100°W, 15°N-15°S, c) 150°E-100°W, 25°N-25°S, d) 150°E-100°W, 30°N-30°S, and e) 0-360°, 25°N-25°S, stippled where a *t* test yields grid points significant at or above the 99% confidence level.

Supplementary:

Fig. s1 a) Zonal wind, b) zonal wind reconstructed from geopotential height at 1000mb, c) zonal wind baroclinic component reconstructed from baroclinic geopotential height at 1000mb, d) zonal wind barotropic component reconstructed from barotropic geopotential height at 1000mb from NCEP-NCAR reanalysis *annual* regression onto Niño3.4, with a two-tailed *t* test applied to the regression values and stippled at 99% confidence. The reconstructed wind is a solution to the equations $-\varepsilon u + fv = -\partial_x \phi$ and $-\varepsilon v - fu = -\partial_y \phi$, forced by the specified 1000 mbar geopotential, where an assumed bulk damping due to surface stress is used, with a value ε =(1day)$^{-1}$.

Fig. s2 a) Surface wind, b) surface wind reconstructed from geopotential height at 1000mb, c) surface wind baroclinic component reconstructed from baroclinic geopotential height at 1000mb, d) surface wind barotropic component reconstructed from barotropic geopotential height at 1000mb from NCEP-NCAR reanalysis *annual* regression onto Niño3.4. The units are m s^{-1}.

Fig. s3 a) SLP (Pa °C^{-1}), b) SLP baroclinic component (Pa °C^{-1}), c) SLP barotropic component (Pa °C^{-1}), d) tropospheric temperature (K °C^{-1}), and e) precipitation (mmday^{-1} °C^{-1}) from a 20yr QTCM run with real-time SSTs *annual* regression onto Niño3.4, with a two-tailed *t* test applied to the regression values and stippled at 99% confidence.

Fig. s4 a) SLP anomalies (Pa), b) SLP anomalies baroclinic component (Pa), c) SLP anomalies barotropic component (Pa) associated with ENSO from QTCM control run in Fig. 8a, stippled where a *t* test yields grid points significant at or above the 99% confidence level.

Fig. s5 QTCM barotropic Rossby wave source anomalies associated with ENSO from QTCM control run in Fig. 8a. a) Total, b) shear advection, c) surface drag baroclinic component, and d) vertical advection, stippled where a *t* test yields grid points significant at or above the 99% confidence level. See text for description of each term.

Supplementary:

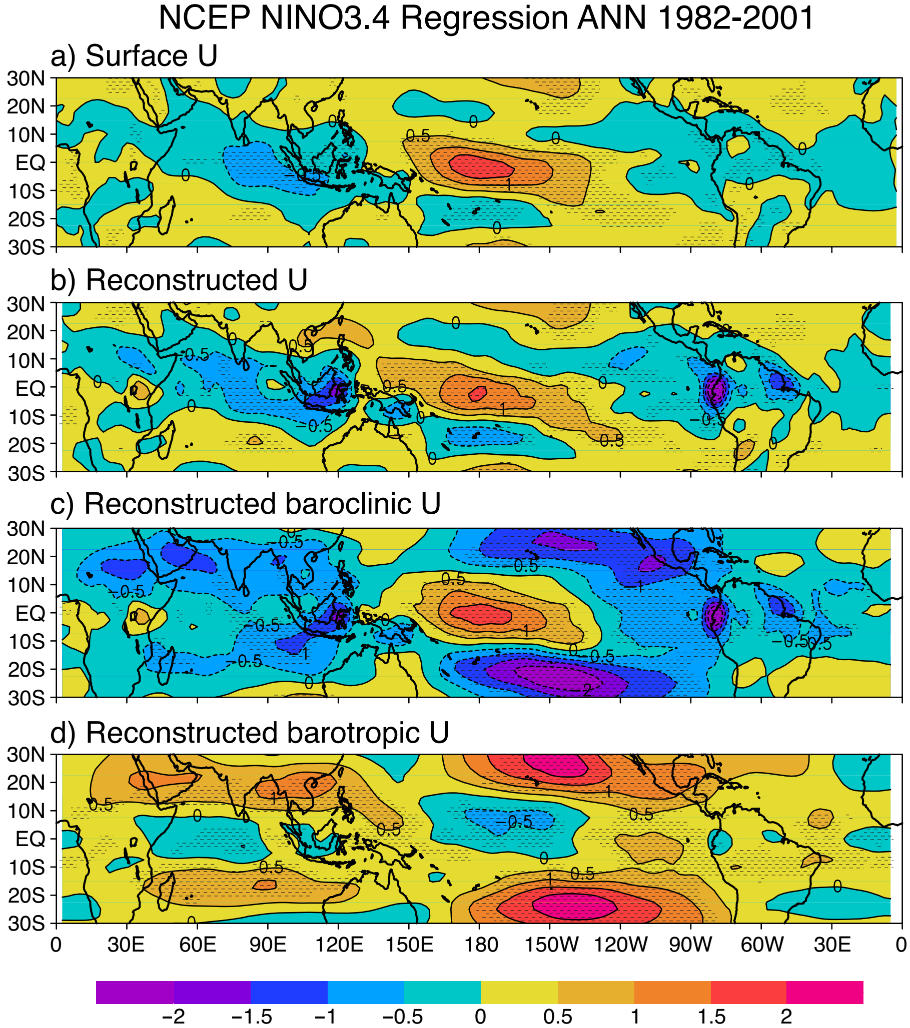

Fig. s1 a) Zonal wind, b) zonal wind reconstructed from geopotential height at 1000mb, c) zonal wind baroclinic component reconstructed from baroclinic geopotential height at 1000mb, d) zonal wind barotropic component reconstructed from barotropic geopotential height at 1000mb from NCEP-NCAR reanalysis *annual* regression onto Niño3.4, with a two-tailed *t* test applied to the regression values and stippled at 99% confidence. The reconstructed wind is a solution to the equations $-\varepsilon u + fv = -\partial_x \phi$ and $-\varepsilon v - fu = -\partial_y \phi$, forced by the specified 1000 mbar geopotential, where an assumed bulk damping due to surface stress is used, with a value ε =$(1\text{day})^{-1}$.

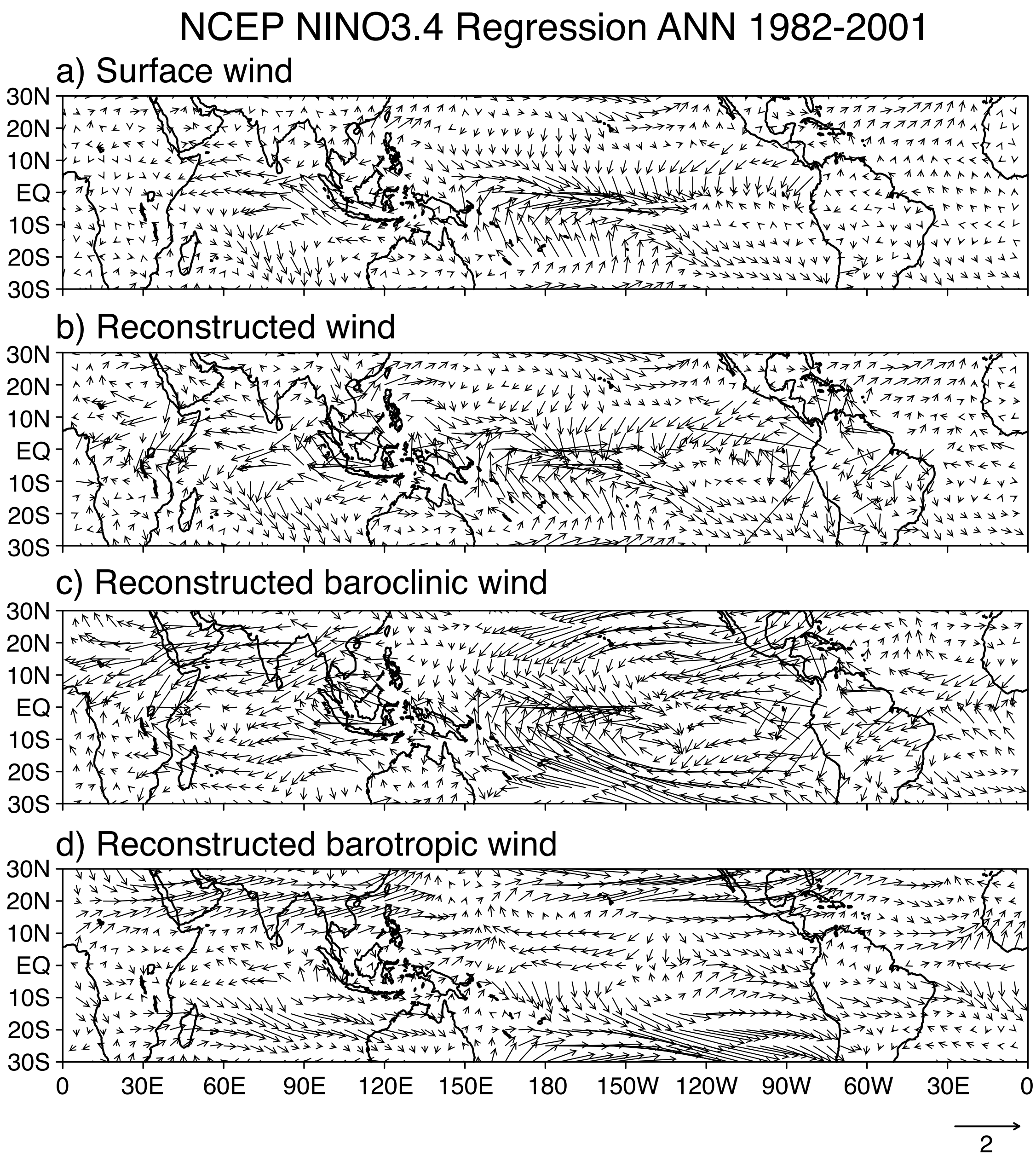

Fig. s2 a) Surface wind, b) surface wind reconstructed from geopotential height at 1000mb, c) surface wind baroclinic component reconstructed from baroclinic geopotential height at 1000mb, d) surface wind barotropic component reconstructed from barotropic geopotential height at 1000mb from NCEP-NCAR reanalysis *annual* regression onto Niño3.4. The units are m s^{-1}.

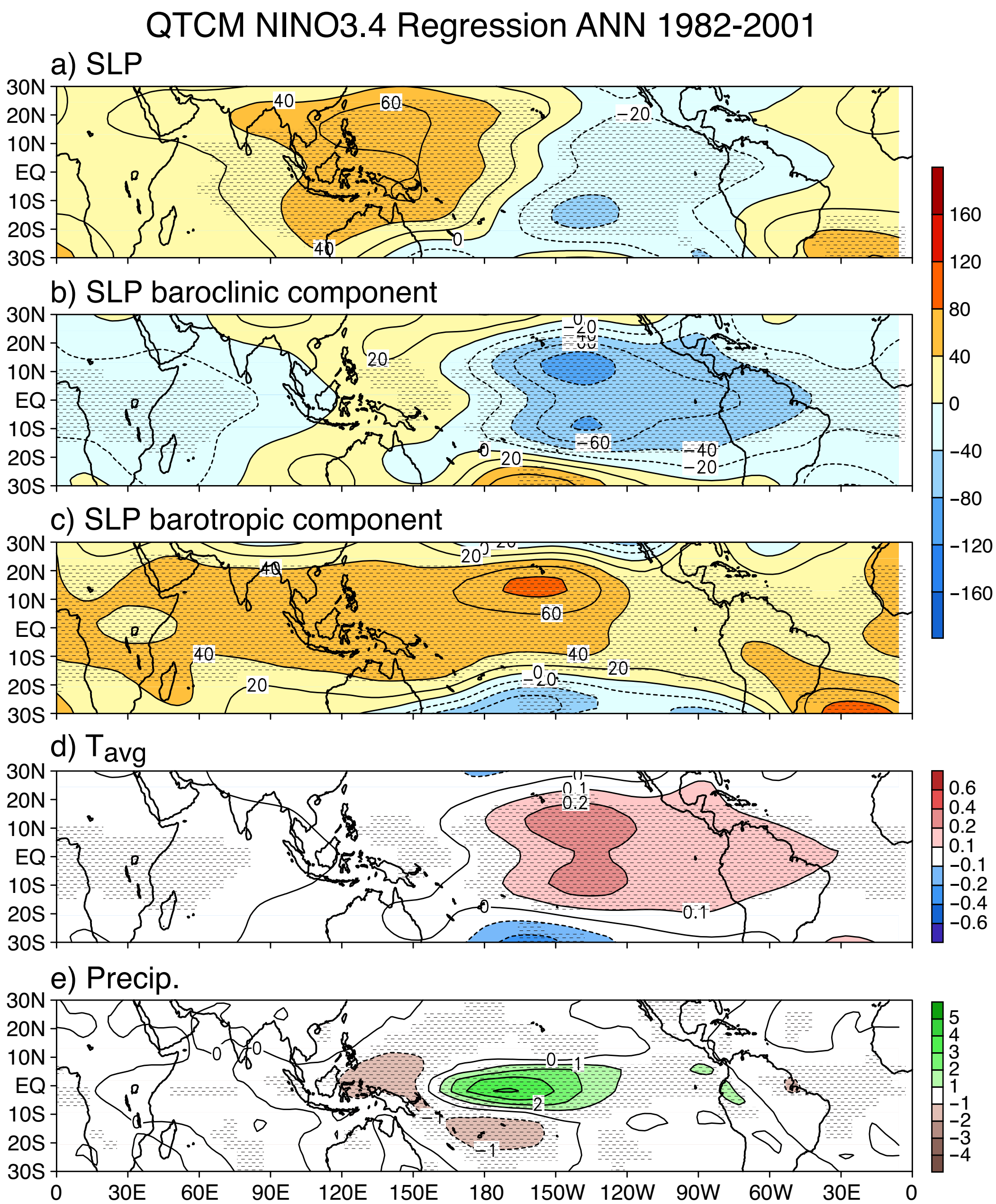

Fig. s3 a) SLP (Pa $°C^{-1}$), b) SLP baroclinic component (Pa $°C^{-1}$), c) SLP barotropic component (Pa $°C^{-1}$), d) tropospheric temperature (K $°C^{-1}$), and e) precipitation (mmday^{-1} $°C^{-1}$) from a 20yr QTCM run with real-time SSTs *annual* regression onto Niño3.4, with a two-tailed *t* test applied to the regression values and stippled at 99% confidence.

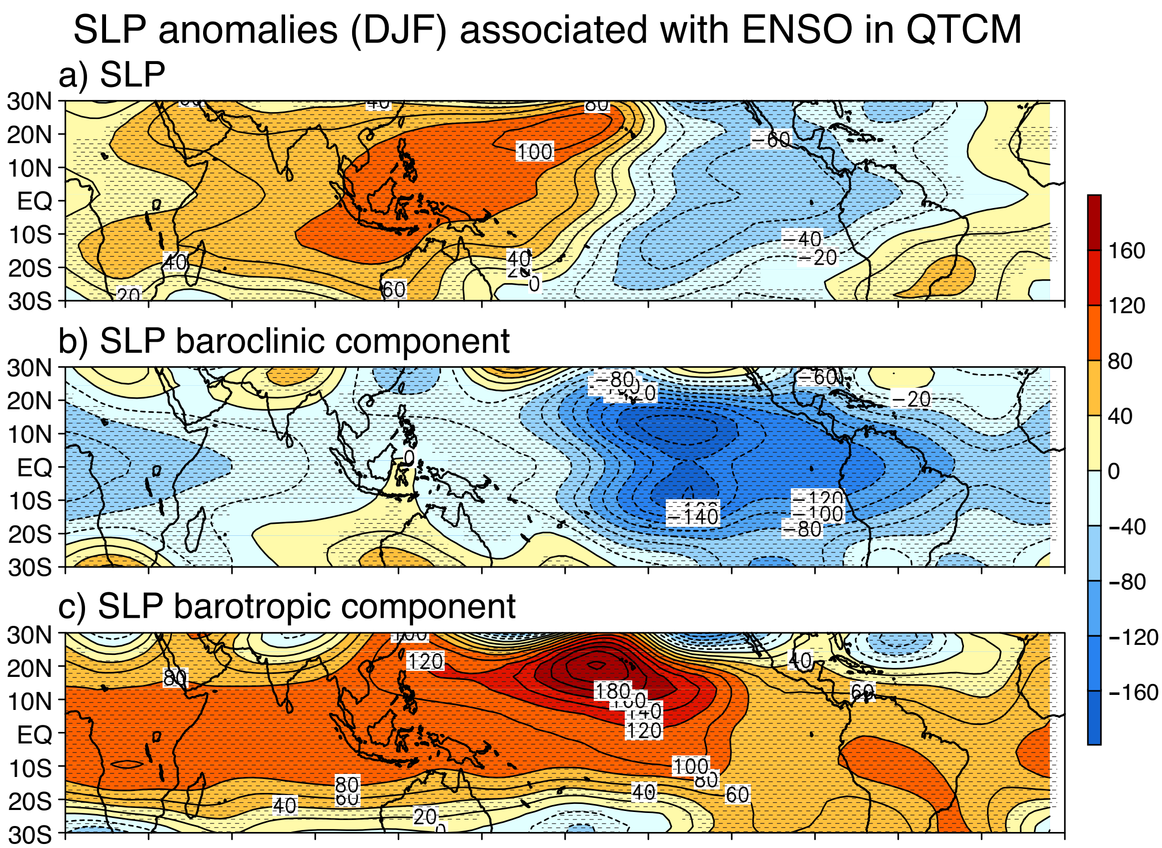

Fig. s4 a) SLP anomalies (Pa), b) SLP anomalies baroclinic component (Pa), c) SLP anomalies barotropic component (Pa) associated with ENSO from QTCM control run in Fig. 8a, stippled where a *t* test yields grid points significant at or above the 99% confidence level.

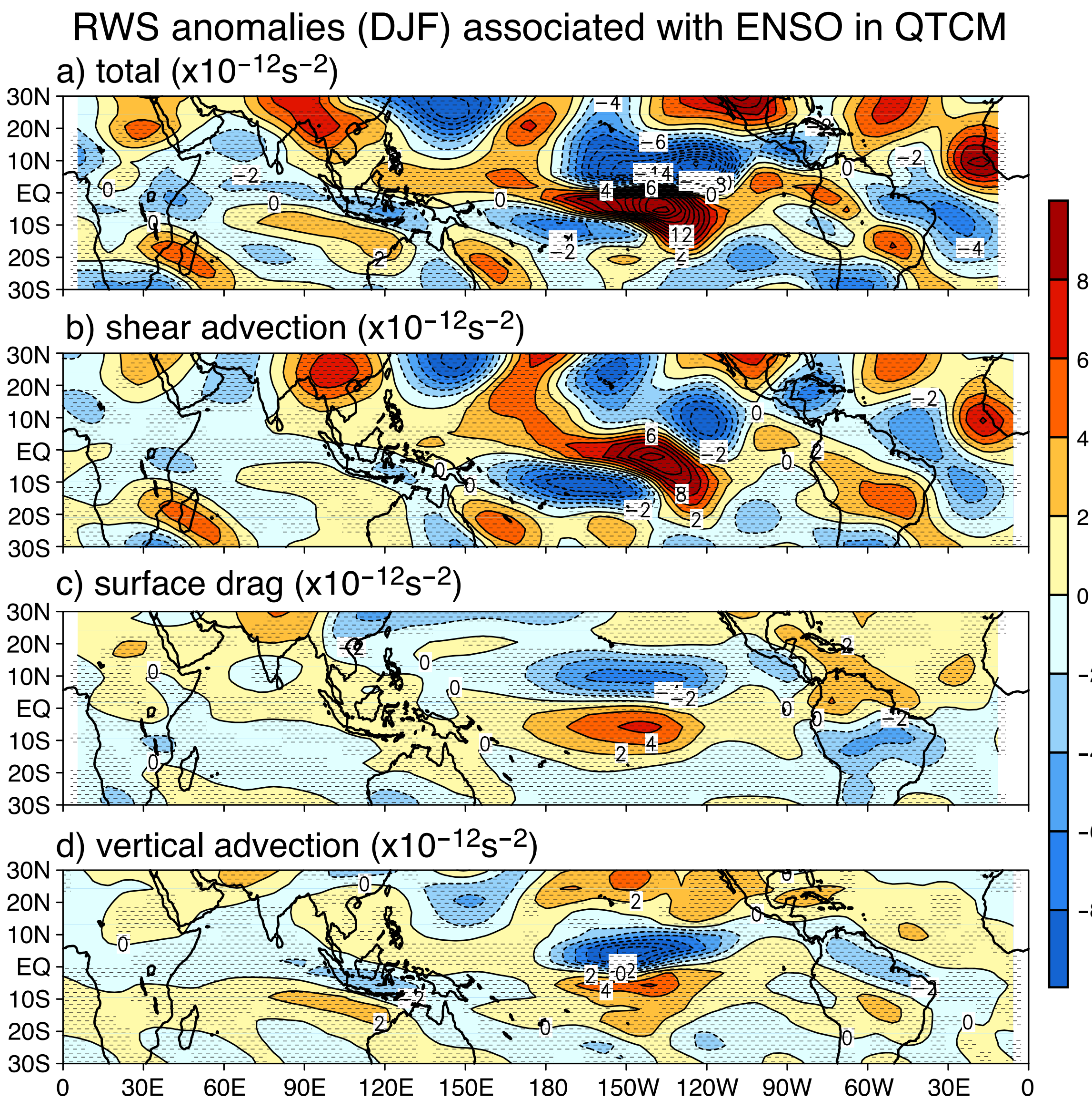

Fig. s5 QTCM barotropic Rossby wave source anomalies associated with ENSO from QTCM control run in Fig. 8a. a) Total, b) shear advection, c) surface drag baroclinic component, and d) vertical advection, stippled where a *t* test yields grid points significant at or above the 99% confidence level. See text for description of each term.